








RESEARCH ARTICLE | MARCH 05 2024

Influence of thickness scaling on the electronic structure and optical properties of oxygen deficient BaBiO_{3-5} thin films grown on SrTiO_3 -buffered $\text{Si}(001)$ substrate

I. Ahmed ; M. Korytov ; S. Sergeant ; T. Nuytten ; T. Conard ; S. De Gendt ; C. Merckling 



APL Mater. 12, 031105 (2024)

<https://doi.org/10.1063/5.0188209>



Articles You May Be Interested In

Strain induced modification in physical properties of charge-ordered insulator BaBiO_3 thin films

AIP Conf. Proc. (October 2019)

Epitaxial growth of the candidate ferroelectric Rashba material SrBiO_3 by pulsed laser deposition

APL Mater. (March 2023)

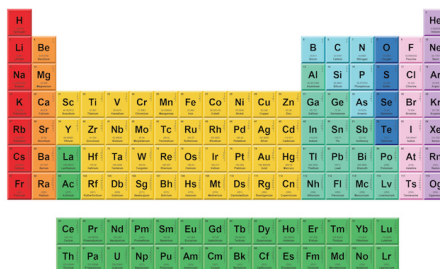
Influence of sintering temperature on the tetragonal structure of $\text{BaPb}_{0.7}\text{Bi}_{0.3}\text{O}_3$

AIP Conf. Proc. (February 2024)



THE MATERIALS SCIENCE MANUFACTURER®

Now Invent.™



American Elements
Opens a World of Possibilities

...Now Invent!

www.americanelements.com

© 2021-2024 American Elements & U.S. Registered Trademark

Influence of thickness scaling on the electronic structure and optical properties of oxygen deficient $\text{BaBiO}_{3-\delta}$ thin films grown on SrTiO_3 -buffered $\text{Si}(001)$ substrate

Cite as: APL Mater. 12, 031105 (2024); doi: 10.1063/5.0188209
Submitted: 20 November 2023 • Accepted: 18 February 2024 •
Published Online: 5 March 2024



View Online



Export Citation



CrossMark

I. Ahmed,^{1,2,a)} M. Korytov,² S. Sergeant,² T. Nuytten,² T. Conard,² S. De Gendt,^{2,3} and C. Merckling^{1,2}

AFFILIATIONS

¹Department of Materials Engineering, KU Leuven, Kasteelpark Arenberg 44, 3001 Leuven, Belgium

²Imec, Kapeldreef 75, 3001 Leuven, Belgium

³Department of Chemistry, KU Leuven, Celestijnenlaan 200F, 3001 Leuven, Belgium

^{a)}Author to whom correspondence should be addressed: islam.ahmed@imec.be

ABSTRACT

BaBiO_3 has attracted a lot of research attention since it was discovered as the parent compound for the high- T_c superconducting $\text{BaPb}_x\text{Bi}_{1-x}\text{O}_3$ and $\text{Ba}_{1-x}\text{K}_x\text{BiO}_3$. In its pure state, BaBiO_3 is an insulator due to the presence of a breathing distortion of the BiO_6 octahedra. The distortion is attributed to the valency of Bi in the compound being charge-ordered in the form of Bi^{3+} and Bi^{5+} along the lattice, resulting in alternating expanded or contracted BiO_6 octahedra. The interaction between the electronic properties and the thickness of the thin film is crucial to study. We conducted a thorough study to investigate the effect of the thickness reduction of $\text{BaBiO}_{3-\delta}$ grown on SrTiO_3 -buffered Si substrates on the optical properties as well as the Bi electronic structure of the thin films. We conclude that modifications in the valency of Bi in the ultra-thin film regime result in an optically conducting layer.

© 2024 Author(s). All article content, except where otherwise noted, is licensed under a Creative Commons Attribution (CC BY) license (<http://creativecommons.org/licenses/by/4.0/>). <https://doi.org/10.1063/5.0188209>

I. INTRODUCTION

The perovskite structure, with the chemical formula ABO_3 , has allowed for exploring a variety of interesting physics such as ferroelectricity,¹ magnetism,² and superconductivity.³ In this representation, the B cation is octahedrally coordinated by oxygen ions, forming a network of BO_6 across the crystal, which contributes to shaping the material's overall band structure. Structural distortions of the octahedra, therefore, play a crucial role in defining the electronic and magnetic properties of the perovskites. BaBiO_3 (BBO_3) has been studied for its use in applications such as photovoltaics,⁴ photocatalysis for water splitting,⁵ and superconducting devices,⁶ and it is well represented by this phenomenon. BBO_3 has a unique phase diagram where it undergoes a phase transition at 430 K from monoclinic in space group $C2/m$ to rhombohedral in space group $R\bar{3}$ and finally to a cubic structure in space group $Pm\bar{3}m$ above 820 K.⁷

At room temperature, according to neutron profile measurements, the monoclinicity of BBO_3 is crystallographically characterized by having two distinguishable Bi-O bond lengths of 2.12 to 2.28 Å, forming a charge density wave (CDW).⁸ The insulating or metallic behavior of BBO_3 has been widely attributed to the structural properties of the perovskite and the presence or absence of CDW in the BBO_3 lattice.

In the ionic model, the charge disproportionation over the Bi ions has been considered for the material to have a chemical formula of $\text{Ba}_2\text{Bi}^{+3}\text{Bi}^{+5}\text{O}_6$. The charge ordering is associated with a static breathing lattice distortion where Bi resides within expanded and contracted octahedra in an alternating fashion. According to band theory, BBO_3 is expected to be metallic with its half-filled valence band; however, the above-mentioned distortions are responsible for opening an energy gap in the conduction band, rendering the material a Peierl's insulator with an optical gap

of 1.85–2.05 eV.^{9–13} However, as a result of the experimental observation of no distinction among the valency of the two crystallographically inequivalent Bi ions, another bond disproportionation image came into the picture.^{14–17} In this regime, the strong hybridization between Bi 6s and O 2p orbitals excludes the charge ordering in favor of having only Bi³⁺ in the structure; therefore, one oxidation state but different local environments.^{18–20} The neutron diffraction data and charge neutrality are then justified by an unequal transfer of charge from O 2p to the two distinct Bi states.¹⁵

Research interest has been devoted to the parent material since the discovery of its superconductivity upon *p*-type doping. At $x = 0.3$ and 0.4, respectively, BaPb_xBi_{1-x}O₃ and Ba_{1-x}K_xBiO₃ become superconducting, where a phase transition to a cubic structure occurs, which recovers the expected metallicity of the oxide.^{21,22} This phase transition is characterized by the suppression of the characteristic symmetric A_{1g} Raman-active mode observed for the pristine material around 570 cm⁻¹, which is attributed to the breathing phonon mode.²³ Confinement of the material in thin films has been alternatively investigated to understand the link between the structural and electronic properties of BBO₃ without chemically altering the composition. Thickness induced metal-to-insulator transition for SrVO₃,²⁴ LaNiO₃,²⁵ and SrIrO₃²⁶ is a relevant example for the interplay between the electronic properties and the structural transition in perovskite materials. Kim *et al.* studied the effect of reducing the film thickness on both the structural and optical properties of BBO₃.²⁷ A phase transition to a cubic structure driven by the suppression of breathing distortion, which is characterized by the absence of the characteristic Raman-active mode for BBO₃ upon thickness reduction, was observed. However, the electrical transition to a metallic system for an ultra-thin film has not yet been demonstrated. More recent studies followed, where modifications to the electronic and optical properties are obtained by reducing the thickness of the BBO₃ thin films grown on SrTiO₃ (STO) substrates by pulsed laser deposition (PLD),^{28,29} but without a conclusion on the driving force of this effect.

In this work, we performed spectroscopic characterization on BaBiO_{3-δ} (BBO_{3-δ}) thin films epitaxially grown by molecular beam epitaxy (MBE) on STO-buffered Si substrates. This is to understand the origin of the lattice distortion and how confinement alters the physical and optical properties of BBO_{3-δ} thin films.

II. EXPERIMENTAL

BBO_{3-δ} thin films of different thicknesses are grown in an ultra-high vacuum oxide chamber of a Riber 49 MBE reactor on Si(001) substrates with 15 nm STO buffer layers. A detailed description of the MBE adsorption-controlled growth process can be found in our previous study,³⁰ where a Bi-rich environment along with plasma oxygen are used to ensure the epitaxy of the volatile BiO species. The sample is then cooled down in oxygen for a short time before being transferred to the loadlock. Reflection high-energy electron diffraction (RHEED) with a 20 kV operated e-gun is utilized to monitor the thin films' growth mode and morphology. For the crystal perfection assessment, a Phillips X'Pert Panalytical high resolution x-ray diffraction (HR-XRD) setup is used. Symmetric ω–2θ scans based on the Cu K_{α1} radiation line (λ ≈ 15.4 Å) are collected from an 18° scattering angle up to 35.2°. The crystalline quality of the films

is evaluated by the full width at half-maximum (FWHM) of each layer's rocking curve (RC) peak. To investigate the effect of thickness scaling on the properties of the layers, MBE is used to grow films that are 3, 4, 25, and 47 nm thick, as measured by the x-ray reflectivity (XRR) technique.

Raman spectra are gathered upon exciting the heterostructures with 633 nm laser light on the Horiba Jobin-Yvon LabRAM HR800 Raman tool in backscattering configuration. Photoluminescence (PL) response at room temperature is also collected on the same tool with an excitation laser of 532 nm. X-ray photoemission spectroscopy (XPS) for the thin films is performed with monochromatized Al K_{α1} radiation (beam energy of 1486.6 eV) in the angle integrated mode using a Physical Electronics QUANTES instrument. The optical constants of the different thin films are calculated based on spectroscopic ellipsometry (SE) measurements performed on a J. A. Woollam RC2. CompleteEASE software is used for fitting the obtained data. For transmission electron microscopy (TEM) inspection, a Titan tool is used with an operating voltage of 200 kV. Lamella is prepared by using a focused ion beam (FIB) with reduced ion current, and no scanning electron microscopy (SEM) is carried out while preparing the sample. A capping layer of 3 nm of Al₂O₃ is deposited *in situ* to protect the sample from degradation while being measured.

III. RESULTS AND DISCUSSIONS

Figure 1(a) illustrates a high-angle annular dark-field (HAADF) scanning-TEM (STEM) image of the STO buffer layer as well as the 25 nm BBO_{3-δ} layer with atomic resolution ($Z_{\text{Ba}} = 56$, $Z_{\text{Bi}} = 83$). Due to the 11.7% lateral lattice mismatch between the active layer and buffer layer, BBO_{3-δ} growth is achieved via domain matching epitaxy, where each 8 unit cell is accommodated on 9 unit cells of STO.^{31,32} This is clearly visible in Fig. S1 based on the fast Fourier transform (FFT) filtered image and the RHEED pattern evolution at the interface as compared to that of the surface after cooling down. The epitaxial relationship of STO(001)||BBO(001), as seen in Figs. 1(c) and 1(d), is achieved without the use of a buffer layer of BaO, as was previously reported.³³ Energy dispersive x-ray spectroscopy (EDS) is used to study the composition of the epilayers; a quantified profile averaged along the growth direction is shown in Fig. 1(b). A drop in the oxygen signal within BBO_{3-δ} with respect to the STO layer is observed. This observation is attributed to a lower oxygen content in the BBO_{3-δ} layer. Besides, a periodic modulation within the BBO_{3-δ} epilayer can be noticed in every three perovskite unit cells along the growth direction, as the intensity is varied, in the HAADF-STEM image. Ordered oxygen vacancies are common among other oxygen deficient perovskite oxides such as SrFeO₃³⁴ and SrCoO₃.³⁵ Therefore, oxygen deficiency within BBO_{3-δ} is assumed to form an ordered oxygen vacancy superlattice. The superstructure, resulting from the ordered oxygen vacancies, is also manifested by the doubly spotty pattern in the reciprocal space image of BBO_{3-δ} as compared to the single diffraction spot of STO, as highlighted by the blue and green ovals in Figs. 1(c) and 1(d), respectively.

Figure 2(a) depicts the out-of-plane symmetric scans for the different samples of BBO_{3-δ} with thicknesses of 3, 4, 25, and 47 nm. Scans are calibrated based on the Si(004) Bragg reflection. The STO(002) Bragg reflection from the buffer is observed for the four

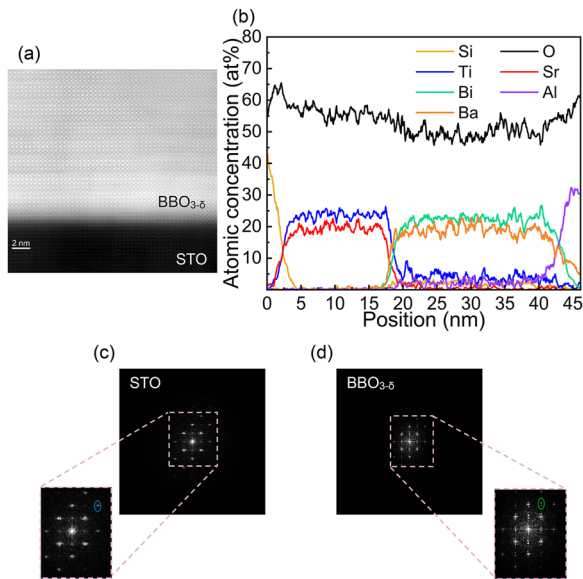


FIG. 1. (a) HAADF-STEM image showing the heterostructure of the STO buffer layer and 25 nm $\text{BBO}_{3.8}$ thin film, (b) EDS profile quantified throughout STO, $\text{BBO}_{3.8}$, and Al_2O_3 capping layer, and (c) and (d) reciprocal space images based on the FFT analysis for STO and $\text{BBO}_{3.8}$ with zoomed-in images, respectively.

different samples at $\omega = 23.13^\circ$, and the $\text{BBO}_{3.8}(002)$ reflection is probed at $\omega = 20.66^\circ$ with a strong intensity-to-thickness correlation. Indeed, the diffraction peak is more pronounced for the thicker layers of 25 and 47 nm, while for the 3 and 4 nm films, the diffraction is barely captured in terms of its strength due to the limited thickness and more room for mosaic spread. The lattice constant of the virtual substrate STO is, on average, 3.92 Å. For $\text{BBO}_{3.8}$, the average out-of-plane pseudocubic lattice constant is 4.370 and 4.379 Å for the 25 and 47 nm films, respectively. On the other hand, both layers have almost the same crystalline quality, as determined by the FWHM around 0.6° of the diffraction peaks at the rocking curve configuration. Reflectivity spectra of the combined oscillations from the STO and $\text{BBO}_{3.8}$ layers are shown in the XRR scans, which are used to accurately extract the thickness of the thin films based on the Fourier transform of the signals and then calculate the growth rate of the layers to be 1.2 nm/min. Figure 2(c) schematically illustrates the heterostructure grown on a Si(001) substrate alongside the RHEED patterns recorded after the full growth of the layers is accomplished. The streak-to-streak distance denotes the formation of the perovskite, as referred to in our previous study.³⁰ The streaky patterns ensure a layer-by-layer growth mechanism with smooth surfaces for all films. In addition, the 25 and 47 nm RHEED patterns show that a $\times 6$ surface reconstruction along (110) is taking place.

Tilting of the BiO_6 octahedra around the pseudocubic [110] axis is taking place to stabilize the structure in the presence of the breathing lattice distortion.³⁶ This enables the lowering of the symmetry of the structure from a cubic to a monoclinic structure at room temperature and the doubling of the unit cell. Even though the diffraction peak of $\text{BBO}_{3.8}$ is observed at a position close to that expected for a cubic structure, it is not straightforward to assume

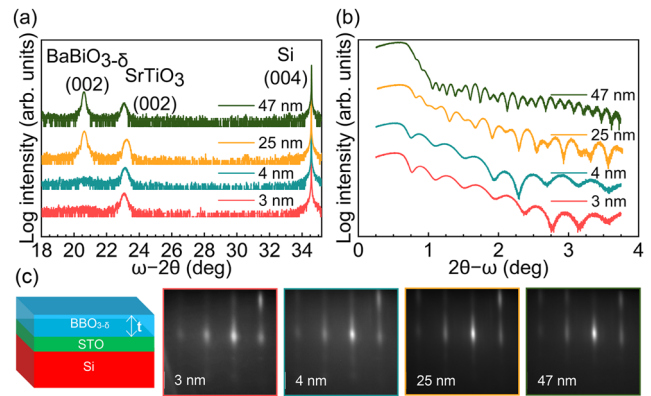


FIG. 2. (a) XRD's out-of-plane ω - 2θ scans showing Si substrate, STO buffer layer, and $\text{BBO}_{3.8}$ diffraction peaks for the different $\text{BBO}_{3.8}$ thin films, (b) XRR scans showing thickness oscillations due to the STO buffer and $\text{BBO}_{3.8}$ active layer, and (c) schematic diagram showing the heterostructure grown on Si(001) substrate and the streaky RHEED patterns for the four thin films.

that the structure is cubic. This is due to the fact that the lowering of symmetry is mainly occurring because of oxygen movements, and XRD diffraction is governed by planes containing heavier atoms like those of Ba and Bi in the structure, which makes it more difficult to differentiate between the two structures by simple out-of-plane symmetric scans. However, for convenience, pseudocubic Miller indices are assigned to the diffraction peaks.

As illustrated in Fig. 3(a), the Raman spectra for the different samples are plotted and compared with a Si reference spectrum. An intense peak can be observed at a phonon frequency of 521 cm^{-1} , corresponding to the Raman-active mode of the Si substrate. An additional peak at a phonon frequency of 565 cm^{-1} corresponds to the phonon breathing mode existing for BBO_3 with long range A_{1g} symmetry.²³ Normalizing the spectra relative to the substrate Raman mode allows for a more qualitative view of the Raman response of the $\text{BBO}_{3.8}$ layers. This dominant Raman peak for $\text{BBO}_{3.8}$ is observed for film thickness between 4 and 47 nm; however, it is completely vanishing for the 3 nm film. If the 3 nm film is expected to show lower intensity due to the low Raman cross-section, the complete absence of the Raman peak indicates a different response

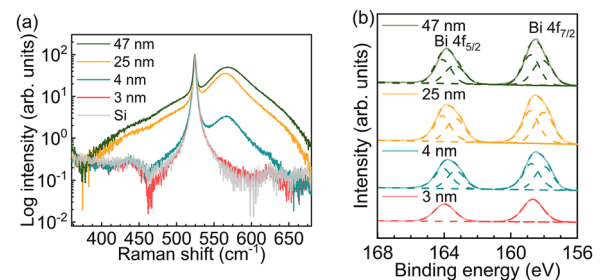


FIG. 3. (a) Raman spectra for the different samples showing the characteristic Raman-active modes for Si and $\text{BBO}_{3.8}$ thin films at 521 and 565 cm^{-1} , respectively, and (b) XPS measurements of the Bi 4f core-level with different film thicknesses.

than that of the 4 nm thin films. While an ideal cubic perovskite does not have Raman-active modes according to the polarization selection rules, this suggests that our films have a lowered symmetry due to the breathing distortion of the lattice, which is not persistent at a thickness of 3 nm. Similarly, in K-doped BBO₃ sputtered film, at the composition of the cubic phase, the Raman peak is not observed and is accompanied by an insulating-to-metal transition.²³

Since this breathing distortion of BBO₃ has been linked to the presence of two oxidation states for bismuth (being a valence skipping element), the Bi 4*f* XPS core-level spectra for the set of samples are collected and shown in Fig. 3(b). As BBO₃ oxide is known to be an insulating material, charge neutralization is needed for carrying out the XPS measurements. To compare the oxidation states, all collected spectra are binding energy calibrated according to a fixed C 1*s* binding energy. For 4, 25, and 47 nm, thin films have the same line shape, which is fitted by two doublets. Each doublet represents an electronic angular momentum (*j* = 5/2 and 7/2) of Bi 4*f* core-level with an energy splitting of 5.3 eV. The peak fitting is then carried out using Casa XPS software with a mixed Gaussian–Lorentzian peak shape. Utilizing two doublets refers to the obvious presence of two different oxidation states with an energy separation of 0.75 eV. However, for the thinnest 3 nm film, there is only one oxidation state according to the fitting, as shown in Table I.

Bismuth can exist in different oxidation states for the various compounds: Bi³⁺ for BiFeO₃ and Bi₂O₃, Bi⁵⁺ for NaBiO₃ and Bi₂O₅, and sometimes even a mixture of Bi³⁺ and Bi⁵⁺ like for Bi₂O₃–Ga₂O₃ and CaBiO₃.^{37–41} In the literature, the average values for the binding energies for different Bi-containing compounds and BBO₃ are Bi³⁺ 4*f*_{7/2} = 158.1 eV and Bi⁵⁺ 4*f*_{7/2} = 158.8 eV.^{17,42,43} With a separation of 0.75 eV between the two peaks, the values according to the deconvolution shown in Table I suggest two distinct oxidation states, which are Bi⁵⁺ and Bi³⁺, agreeing with the widely known ordered perovskite formula of Ba₂ Bi⁵⁺Bi³⁺O₆. This is, however, not observed for the 3 nm film, where one oxidation state, Bi⁴⁺, exists with a binding energy between those of Bi³⁺ and Bi⁵⁺, as shown in Table I. Only one oxidation state for Bi 4*f*'s core-level is also evident by the symmetric line shape of the peak measured as well as the shorter FWHM of the peak, as illustrated in Table S1. The origin of the breathing distortion in some cases is related to the

charge ordering; however, in the literature, there is limited evidence of mixed valency for BBO₃.^{44,45} Zapf *et al.* related the distinction of the Raman-active mode to the presence of a dead layer that does not host the breathing distortion below 3 nm thickness.²⁹ Yet, our XPS data show a strong correlation between the breathing distortion, hence the Raman response, and the electronic structure of the thin film.

To further investigate the effect of the different electronic structures on the optical conductivity of the thin films, SE measurements were carried out. Optical conductivity of the different thin films is calculated using the refractive index (*n*) and absorption coefficient (*k*) as extracted from the SE measurements with a range of wavelengths from 500 up to 1240 nm. Figure 4(a) shows how the layers are absorbing the light excitation with a peak centered around 2.1 eV for 4, 25, and 47 nm, which does not exist for the 3 nm film. This response has been linked in the literature to the CDW, which is attributed to the breathing distortion of the BiO₆ octahedra and the strong hybridization of the Bi 6*s* and O 2*p* orbitals.⁴⁶ The CDW generates a density of states above and below the material's Fermi level, resulting in this absorption peak in optical conductivity. This justifies the noticeable increase in the spectral intensity of the Raman response of the 25 nm layer when excited with a laser of 633 nm wavelength compared to other lasers with wavelengths of 785, 532, and 405 nm, as shown in Fig S2. This, as pointed out previously,²³ is because the laser radiation is in resonance with the optical bandgap of BBO_{3,δ}, which is around 2.1 eV. The intensities of BBO_{3,δ}'s Raman peak as well as optical conductivity at a photon energy of 2.1 eV for the different samples are plotted against the thickness of the layer, as shown in Fig. 4(b). The abrupt decrease in the signals going from a thickness of 4 nm down to 3 nm indicates that the effect is beyond the spectroscopic information due to the limited measured volume.

In Fig. 4(c), the PL responses of the BBO_{3,δ} layers are shown and compared to a Si reference spectrum at room temperature with a range from 560 to 830 nm. PL spectra of 25 and 47 nm thin films show a sharp peak (P₅) with a FWHM of 5.17 and 6.71 nm and positions of 565.70 and 565.79 nm (2.19 eV), respectively. In addition, according to the fitting of the data after subtracting the background shown in Fig. S3, there is a broad emission peak (P₁) around 640 nm (1.94 eV) with a FWHM of 99.27 and 95.71 for the 25 and 47 nm thin films, respectively. Other peaks are also observed (P₄, P₃, P₂),

TABLE I. Bi 4*f*'s core-level illustrating the binding energies of the different oxidation states for the four BBO_{3,δ} thin films.

	Bi core-level	Binding energy (eV)					
		4 <i>f</i> _{5/2}			4 <i>f</i> _{7/2}		
		Bi ⁵⁺	Bi ⁴⁺	Bi ³⁺	Bi ⁵⁺	Bi ⁴⁺	Bi ³⁺
Thickness (nm)	47	164.1		163.3	158.78		158.0
	25	164.0		163.3	158.7		158.0
	4	164.0		163.3	158.7		158.0
	3		163.78			158.5	

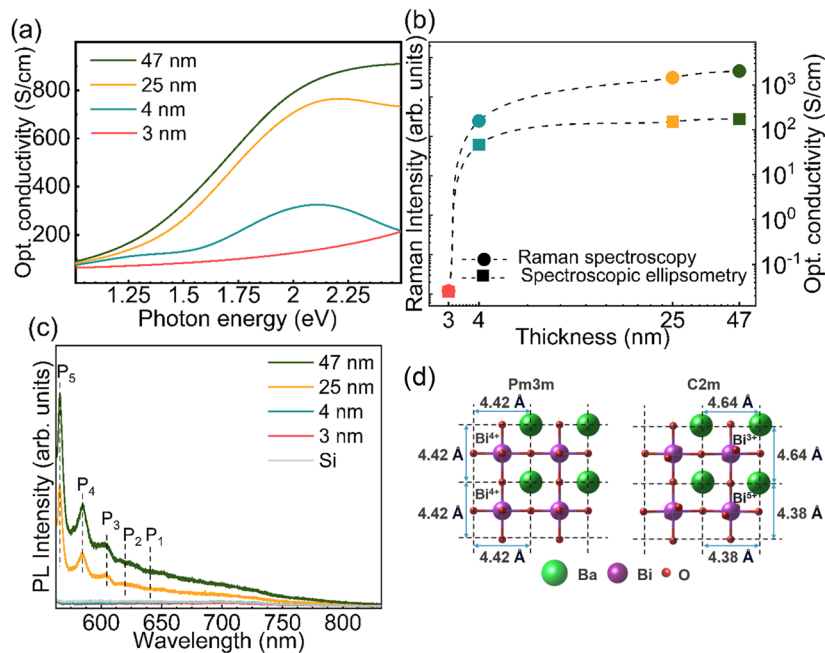


FIG. 4. (a) Optical conductivity of the thin films as extracted from SE optical constants data, (b) spectral intensity for both Raman spectra at 565 cm^{-1} and optical conductivity at 2.1 eV showing the vanished intensity for the 3 nm film, as indicated by the same color codes from (a) and (c) PL spectra for the different films, and (d) schematic diagram showing the Pm3m cubic structure of $\text{BaBi}^{4+}\text{O}_3$ as well as the charge ordered monoclinic C2m structure of $\text{Ba}_2\text{Bi}^{3+}\text{Bi}^{5+}\text{O}_6$.

corresponding to energies of 2.12 , 2.06 , 2 , and 1.94 eV , respectively. Extracted information from fitting the PL data can be found in Table II.

The sharpest peak in the spectra around 2.19 eV is assigned to the band-to-band radiative transition, hence corresponding to the optical bandgap of the compound, agreeing with previously reported data for the direct bandgap of BBO_3 .^{4,47,48} As observed before for BBO_3 nanoparticles,⁴⁹ wide emission spectra can be related to the presence of defects within the samples, specifically doubly charged oxygen vacancies, V_0^{++} , which are responsible for the yellow emission with a range of $550\text{--}610\text{ nm}$.⁵⁰ The presence of the broad emission peak around 640 nm is attributed to the presence of Bi^{3+} in the thin films, which causes this redshift.⁵¹ According to a density functional theory (DFT) study, the transition across the bands involves the transfer of photogenerated carriers from the $6s$ orbitals

of Bi^{3+} to the $6s$ orbitals of Bi^{5+} .⁵² So not observing these transitions for the 4 nm thin film is puzzling, and further understanding can be gained by collecting PL spectra at lowered temperatures.⁵³

These results along with the different oxidation states observed for the different films indicate that by decreasing the thickness of the film below 4 nm , the breathing distortion is altered, resulting in the original cubic structure with one oxidation state, as shown in Fig. 4(d). Admittedly, we do not yet have the evidence that this film is electrically conductive, and this will be our next research question. Results do not exclude any of the two images but ensure the occurrence of both charge orderings, which results in $\text{Bi } 6s \text{ O } 2p$ hybridization and CDW that are responsible for opening an optical bandgap. With the reduction of the thickness, the charge ordering and the associated breathing distortion are suppressed, and the cubic structure is retrieved within the perovskite portion of the thin film; therefore resulting in the original band structure of BBO_3 with no optical bandgap.

TABLE II. PL spectra peak position and FWHM of each of the peaks of 25 and 47 nm films.

	(nm)	PL fitted peak				
		P ₁	P ₂	P ₃	P ₄	P ₅
47 nm	Position	640.16	619.16	602.96	583.93	565.79
	FWHM	95.71	19.50	13.21	21.87	6.71
25 nm	Position	640.15	619.79	602.81	583.86	565.70
	FWHM	99.27	18.72	12.03	16.19	5.17

IV. CONCLUSIONS

In this work, we shed light on the optical properties of the compound $\text{BaBiO}_{3.6}$ and their link to its structural properties and electronic structure. Even though there are ordered oxygen vacancies within the structure as observed by STEM, the perovskite structural and spectroscopic properties are still observed for the grown thin films. Unlike other interpretations where only Bi^{3+} is present and the disproportionation exists with a hole density on the oxygen site (O^{2-} and O^-),⁵⁴ here it is shown, according to XPS results, that charge disproportionation happens on the Bi site. It is demonstrated

that the suppression of the charge ordering with a thickness lower than 4 nm results in the suppression of the Raman-active mode around 565 cm^{-1} and, hence, the breathing distortion in the BBO_3 lattice. As a result, this closes the optical bandgap, as observed from the spectroscopic ellipsometry data, and retrieves the original band structure of the BaBiO_3 perovskite domains in the thin film with only one oxidation state for Bi ions.

SUPPLEMENTARY MATERIAL

supplementary material includes four subsections: A. Analysis of the STEM image and RHEED pattern, B. Raman intensity as a function of the used excitation wavelength, C. FWHM of XPS peaks for different samples, and D. PL data fitting. In Fig. S1, the FFT filtered STEM image of the 25 nm $\text{BBO}_{3-\delta}$ thin film and RHEED patterns collected at the start of $\text{BBO}_{3-\delta}$ growth and after cooling down the layer illustrate that the growth follows domain matching epitaxy. In Fig. S2, the graph displays how the breathing distortion's Raman peak is changing in intensity as the laser excitation's wavelength is varied. The maximum Raman intensity is shown at a wavelength of 633 nm; the excitation is in resonance with the optical bandgap of the material (2.1 eV) in this case. Table S1 shows the FWHM of the Bi $4f$'s $5/2$ and $7/2$ core-level peaks, which clarifies the motivation behind the fitting used in the graph of Fig. 3(b). In Fig. S3, the PL data is shown with fitted peaks, as described in the Fig. 4 discussion.

ACKNOWLEDGMENTS

This work was part of the IMEC Industrial Affiliation Program. The authors would like to acknowledge process and hardware engineers Hans Costermans and Kevin Dubois for their great support of the MBE cluster tool and Moloud Kaviani, who created Fig. 4(d) using DFT. This research has received funding from the European Research Council (ERC) under the European Union's Horizon 2020 research and innovation program (Grant Agreement No 864483).

AUTHOR DECLARATIONS

Conflict of Interest

The authors have no conflicts to disclose.

Author Contributions

I. Ahmed: Conceptualization (lead); Data curation (equal); Formal analysis (equal); Investigation (lead); Methodology (lead); Visualization (lead); Writing – original draft (lead); Writing – review & editing (equal). **M. Korytov:** Data curation (equal); Formal analysis (equal); Investigation (equal); Methodology (equal); Software (equal); Writing – review & editing (equal). **S. Sergeant:** Data curation (equal); Formal analysis (equal); Methodology (equal). **T. Nuytten:** Formal analysis (equal); Investigation (equal); Methodology (equal); Writing – review & editing (equal). **T. Conard:** Conceptualization (equal); Data curation (equal); Formal analysis (equal); Investigation (equal); Methodology (equal); Writing – review & editing (equal). **S. De Gendt:** Investigation (equal); Resources (equal);

Supervision (equal); Validation (equal); Writing – review & editing (equal). **C. Merckling:** Funding acquisition (lead); Project administration (lead); Resources (lead); Supervision (equal); Validation (equal); Writing – review & editing (equal).

DATA AVAILABILITY

The data that support the findings of this study are available from the corresponding author upon reasonable request.

REFERENCES

- K. J. Choi *et al.*, “Enhancement of ferroelectricity in strained BaTiO_3 thin films,” *Science* **306**(5698), 1005–1009 (2004).
- U. Lüders *et al.*, “Room-temperature magnetism in $\text{LaVO}_3/\text{SrVO}_3$ superlattices by geometrically confined doping,” *Phys. Rev. B* **80**(24), 241102 (2009).
- J. G. Bednorz and K. Alex Müller, “Possible high T_c superconductivity in the Ba-La-Cu-O system,” *Z. Phys. B: Condens. Matter* **64**(2), 189–193 (1986).
- A. S. Chouhan *et al.*, “ BaBiO_3 : A potential absorber for all-oxide photovoltaics,” *Mater. Lett.* **210**, 218–222 (2018).
- J. Tang, Z. Zou, and J. Ye, “Efficient photocatalysis on BaBiO_3 driven by visible light,” *J. Phys. Chem. C* **111**(34), 12779–12785 (2007).
- A. Kussmaul *et al.*, “Superconductor-insulator-superconductor tunneling in $\text{Ba}_{1-x}\text{K}_x\text{BiO}_3$ grain boundaries,” *Appl. Phys. Lett.* **63**(20), 2824–2826 (1993).
- D. E. Cox and A. W. Sleight, “Mixed-valent $\text{Ba}_2\text{Bi}^{3+}\text{Bi}^{5+}\text{O}_6$: Structure and properties vs temperature,” *Acta Crystallogr., Sect. B: Struct. Crystallogr. Cryst. Chem.* **35**(1), 1–10 (1979).
- G. Grüner, “The dynamics of charge-density waves,” *Rev. Mod. Phys.* **60**(4), 1129 (1988).
- S. Tajima *et al.*, “Optical study of the metal-semiconductor transition in $\text{BaPb}_{1-x}\text{Bi}_x\text{O}_3$,” *Phys. Rev. B* **32**(10), 6302 (1985).
- R. P. S. M. Lobo and F. Gervais, “Bismuth disproportionation in BaBiO_3 studied by infrared and visible reflectance spectra,” *Phys. Rev. B* **52**(18), 13294 (1995).
- H. Namatame *et al.*, “Electronic structure and the metal-semiconductor transition in $\text{BaPb}_{1-x}\text{Bi}_x\text{O}_3$ studied by photoemission and x-ray-absorption spectroscopy,” *Phys. Rev. B* **48**(23), 16917 (1993).
- M. Khraisheh, A. Khazndar, and M. A. Al-Ghouthi, “Visible light-driven metal-oxide photocatalytic CO_2 conversion,” *Int. J. Energy Res.* **39**(8), 1142–1152 (2015).
- R. Vesto, H. Choi, and K. Kim, “Observation of bandgap closing in $\text{Sr}_x\text{Ba}_{1-x}\text{BiO}_3$ films: Evidence toward topological order in BaBiO_3 ,” *J. Appl. Phys.* **132**(1), 015102 (2022).
- G. K. Wertheim, J. P. Remeika, and D. N. E. Buchanan, “Electronic structure of $\text{BaPb}_{1-x}\text{Bi}_x\text{O}_3$,” *Phys. Rev. B* **26**(4), 2120 (1982).
- M. Bharath *et al.*, “Interplay of lattice distortion and electronic structure in BaBiO_3 ,” *J. Phys.: Condens. Matter* **32**(5), 055504 (2019).
- J. T. W. De Hair and G. Blasse, “Determination of the valency state of bismuth in BaBiO_3 by infrared spectroscopy,” *Solid State Commun.* **12**(7), 727–729 (1973).
- N. C. Plumb *et al.*, “Momentum-resolved electronic structure of the high- T_c superconductor parent compound BaBiO_3 ,” *Phys. Rev. Lett.* **117**(3), 037002 (2016).
- K. Foyevtsova *et al.*, “Hybridization effects and bond disproportionation in the bismuth perovskites,” *Phys. Rev. B* **91**(12), 121114 (2015).
- A. Khazraie *et al.*, “Oxygen holes and hybridization in the bismuthates,” *Phys. Rev. B* **97**(7), 075103 (2018).
- G. M. Dalpian *et al.*, “Bond disproportionation, charge self-regulation, and ligand holes in s-p and in d-electron ABX_3 perovskites by density functional theory,” *Phys. Rev. B* **98**(7), 075135 (2018).
- A. W. Sleight, J. L. Gillson, and P. E. Bierstedt, “High-temperature superconductivity in the $\text{BaPb}_{1-x}\text{Bi}_x\text{O}_3$ system,” *Solid State Commun.* **88**(11–12), 841–842 (1993).
- L. F. Mattheiss, E. M. Gyorgy, and D. W. Johnson Jr., “Superconductivity above 20 K in the Ba-K-Bi-O system,” *Phys. Rev. B* **37**(7), 3745 (1988).

- ²³S. Tajima *et al.*, “Raman-scattering study of the metal-insulator transition in $\text{Ba}_{1-x}\text{K}_x\text{BiO}_3$,” *Phys. Rev. B* **46**(2), 1232 (1992).
- ²⁴K. Yoshimatsu *et al.*, “Dimensional-crossover-driven metal-insulator transition in SrVO_3 ultrathin films,” *Phys. Rev. Lett.* **104**(14), 147601 (2010).
- ²⁵R. Scherwitzl *et al.*, “Metal-insulator transition in ultrathin LaNiO_3 films,” *Phys. Rev. Lett.* **106**(24), 246403 (2011).
- ²⁶P. Schütz *et al.*, “Dimensionality-driven metal-insulator transition in spin-orbit-coupled SrIrO_3 ,” *Phys. Rev. Lett.* **119**(25), 256404 (2017).
- ²⁷G. Kim *et al.*, “Suppression of three-dimensional charge density wave ordering via thickness control,” *Phys. Rev. Lett.* **115**(22), 226402 (2015).
- ²⁸R. L. Bouwmeester, A. Brinkman, and K. Sothewes, “Thickness-dependent band gap modification in BaBiO_3 ,” *Nanomaterials* **11**(4), 882 (2021).
- ²⁹M. Zapf *et al.*, “Structural and stoichiometric modifications in ultrathin epitaxial BaBiO_3 films,” *Phys. Rev. B* **99**(24), 245308 (2019).
- ³⁰I. Ahmed, S. De Gendt, and C. Merckling, “Self-regulating plasma-assisted growth of epitaxial BaBiO_3 thin-film on SrTiO_3 -buffered Si (001) substrate,” *J. Appl. Phys.* **132**(22), 225304 (2022).
- ³¹M. Zapf *et al.*, “Domain matching epitaxy of BaBiO_3 on SrTiO_3 with structurally modified interface,” *Appl. Phys. Lett.* **112**(14), 141601 (2018).
- ³²J. Narayan and B. C. Larson, “Domain epitaxy: A unified paradigm for thin film growth,” *J. Appl. Phys.* **93**(1), 278–285 (2003).
- ³³T. M. Takehiko Makita and H. A. Hitoshi Abe, “Control of crystal orientation for BaBiO_3 thin film on SrTiO_3 (100) substrate using BaO buffer layer,” *Jpn. J. Appl. Phys.* **36**(2A), L96 (1997).
- ³⁴L. Wang *et al.*, “Brownmillerite phase formation and evolution in epitaxial strontium ferrite heterostructures,” *Appl. Phys. Lett.* **114**(23), 231602 (2019).
- ³⁵Y. Gu *et al.*, “Oxygen-valve formed in cobaltite-based heterostructures by ionic liquid and ferroelectric dual-gating,” *ACS Appl. Mater. Interfaces* **11**(21), 19584–19595 (2019).
- ³⁶B. J. Kennedy *et al.*, “Structures and phase transitions in the ordered double perovskites $\text{Ba}_2\text{Bi}^{\text{III}}\text{Bi}^{\text{V}}\text{O}_6$ and $\text{Ba}_2\text{Bi}^{\text{III}}\text{Sb}^{\text{V}}\text{O}_6$,” *Acta Crystallogr., Sect. B: Struct. Sci.* **62**(4), 537–546 (2006).
- ³⁷O. García-Zaldívar *et al.*, “ BiFeO_3 codoping with Ba, La and Ti: Magnetic and structural studies,” *J. Adv. Dielectr.* **05**(04), 1550034 (2015).
- ³⁸V. Vijaykrishnan, G. U. Kulkarni, and C. N. R. Rao, “Valence states of bismuth and thallium in superconducting cuprates: A Bi- L_3 and Tl- L_3 x-ray absorption spectroscopic study,” *Mod. Phys. Lett. B* **04**(07), 451–461 (1990).
- ³⁹Y. Shimizugawa, N. Sugimoto, and K. Hirao, “X-ray absorption fine structure glasses containing Bi_2O_3 with third-order non-linearities,” *J. Non-Cryst. Solids* **221**(2–3), 208–212 (1997).
- ⁴⁰H. Fan, G. Wang, and L. Hu, “Infrared, Raman and XPS spectroscopic studies of Bi_2O_3 - B_2O_3 - Ga_2O_3 glasses,” *Solid State Sci.* **11**(12), 2065–2070 (2009).
- ⁴¹K. Rokesh, M. Sakar, and T.-O. Do, “Calcium bismuthate (CaBiO_3): A potential sunlight-driven perovskite photocatalyst for the degradation of emerging pharmaceutical contaminants,” *ChemPhotoChem* **4**(5), 373–380 (2020).
- ⁴²M. S. Hegde *et al.*, “Electronic structure of high- T_c $\text{Ba}_{0.6}\text{K}_{0.4}\text{BiO}_3$ by x-ray photoelectron spectroscopy,” *Phys. Rev. B* **39**(7), 4752 (1989).
- ⁴³R. Itti *et al.*, “Photoelectron spectroscopic study of $\text{Ba}_{1-x}\text{Rb}_x\text{BiO}_3$,” *Phys. Rev. B* **43**(1), 435 (1991).
- ⁴⁴L. F. Mattheiss, “Electronic structure of $\text{BaPb}_{1-x}\text{Bi}_x\text{O}_3$,” *Jpn. J. Appl. Phys.* **24**(S2), 6 (1985).
- ⁴⁵H. Namatame *et al.*, “Effects of hole doping and electron-phonon interaction on the electronic structure of $\text{Ba}_{1-x}\text{K}_x\text{BiO}_3$ studied by photoemission spectroscopy,” *Phys. Rev. B* **50**(18), 13674 (1994).
- ⁴⁶H. G. Lee, R. Kim *et al.*, “Anisotropic suppression of octahedral breathing distortion with the fully strained $\text{BaBiO}_3/\text{BaCeO}_3$ heterointerface,” *APL Mater.* **6**(1), 016107 (2018).
- ⁴⁷N. Kumar, S. L. Golledge, and D. P. Cann, “Synthesis and electrical properties of BaBiO_3 and high resistivity BaTiO_3 - BaBiO_3 ceramics,” *J. Adv. Dielectr.* **06**(04), 1650032 (2016).
- ⁴⁸B. Men *et al.*, “Photoluminescence, surface photovoltage and photocatalytic properties of BaBiO_3 powders,” *J. Mater. Sci.: Mater. Electron.* **29**, 12729–12734 (2018).
- ⁴⁹K. V. Shilna, S. C. Sahoo, and K. J. Thomas, “Novel ferromagnetism and negative magnetoresistance in BaBiO_3 nanoparticles,” *Appl. Mater. Today* **27**, 101427 (2022).
- ⁵⁰A. Van Dijken *et al.*, “The luminescence of nanocrystalline ZnO particles: The mechanism of the ultraviolet and visible emission,” *J. Lumin.* **87–89**, 454–456 (2000).
- ⁵¹L. Kumari, J.-H. Lin, and Y.-R. Ma, “Laser oxidation and wide-band photoluminescence of thermal evaporated bismuth thin films,” *J. Phys. D: Appl. Phys.* **41**(2), 025405 (2008).
- ⁵²P. B. Allen and I. B. Bischofs, “Self-trapped exciton defects in a charge density wave: Electronic excitations of BaBiO_3 ,” *Phys. Rev. B* **65**(11), 115113 (2002).
- ⁵³C. J. Ellison *et al.*, “Confinement and processing effects on glass transition temperature and physical aging in ultrathin polymer films: Novel fluorescence measurements,” *Eur. Phys. J. E* **8**, 155–166 (2002).
- ⁵⁴S. Balandeh *et al.*, “Experimental and theoretical study of the electronic structure of single-crystal BaBiO_3 ,” *Phys. Rev. B* **96**(16), 165127 (2017).